Magma ascent and emplacement below floor fractured craters on the Moon from floor uplift and fracture length

D. Walwer, C. Michaut, V. Pinel, M. Adda-Bedia

Version of Record: https://www.sciencedirect.com/science/article/pii/S0031920121000169
Manuscript_199a5949055033639592c50c4c66ad07

Magma ascent and emplacement below floor fractured craters on the Moon from floor uplift and fracture length

D. Walwer[a,*], C. Michaut[a,b], V. Pinel[c], M. Adda-Bedia[d]

[a] *Université de Lyon, Ecole Normale Supérieure de Lyon, Université Lyon 1, CNRS, LGL-TPE, F-69007 Lyon, France*
[b] *Institut Universitaire de France*
[c] *Université Grenoble Alpes, Université Savoie Mont Blanc, CNRS, IRD, IFSTTAR, ISTerre, 38000 Grenoble, France*
[d] *Université de Lyon, Ecole Normale Supérieure de Lyon, Université Claude Bernard, CNRS, Laboratoire de Physique, F-69342 Lyon, France*

Floor fractured craters (FFCs) are a class of craters on the Moon that presents deformed, uplifted and fractured floors. These endogenous modifications were likely caused by the emplacement of underlying magmatic intrusions. Here we provide two independent quantitative observations that reflect how the overpressure leading to a crater-centered intrusion varies as a function of crater radius and crustal thickness: the amount of crater floor uplift and the total length of fractures covering the crater floor. Those two observations can be related to the magma overpressure inside the shallow intrusion provided that a significant part of the elastic energy of deformation associated to magma emplacement below the crater is dissipated by the formation of fractures; a condition that seems to be met for a significant number of craters in the Highlands or at the limit between the Highlands and the lunar maria. Here we show that for those FFCs, variations of these two quantities with crater radius and crustal thickness are well predicted by a process of magma ascent caused by crater unloading. By further developing this model and precising its initial conditions, we show that magma storage in the lunar crust is likely to be in the form of vertical dykes emanating from the crust mantle interface. Finally, this study highlights the use of the total fracture length and fracture patterns on FFCs floors as observations that provide insights into the mechanism of magma ascent and emplacement below FFCs and the characteristics of the encasing medium.

*Corresponding author
Email address: damianwalwer@gmail.com (D. Walwer)

Highlights

- The total length of floor fractures scales with intrusion overpressure.
- Crater floor uplift scales with intrusion overpressure.
- Transport of negatively buoyant magma is triggered by crater unloading.
- Deep crustal magma storage is in the form of vertical dykes.

1. Introduction

Shallow magmatic intrusions such as dykes, sills and laccoliths are important part of volcanic complexes and constitute the building blocks that shape their plumbing systems [6, 34, 44]. Several mechanisms are proposed to explain the emplacement of shallow intrusions and the conditions for which one type of intrusion would prevail over another. Authors have stressed out the role of buoyancy: when the magma reaches its neutral buoyancy depth, it stops to propagate towards the surface and extends laterally, forming a horizontal sill intrusion [63, 24]. The amplitude of non-lithostatic stress components within the crust and associated orientations of principal stresses —influenced by tectonic forces or loads such as volcanic edifices— are also considered as impacting dyke propagation and shallow intrusion emplacement [38, 64, 46, 15]. Propagating dykes tend to open in least compressive stress direction. Horizontal magmatic intrusions can therefore be the result of dyke alignment towards the horizontal maximum compressive stress. Such conditions can be met in compressive tectonic settings or when the surface is unloaded [30, 26]. Other important mechanisms influencing the propagation of magma intrusions involve the role of heterogeneities or inelastic behavior pertaining to the mechanical properties of the host rock such as the layering of sediments, material cohesion and preexisting weaknesses in the crust [56, 55, 42].

Shallow magmatic intrusions are also present on planetary bodies other than Earth [49, 66, 2]. The lunar crust, in particular, seems to be the host of diverse types of magmatic intrusions such as dykes, sills and laccolith [18, 70, 19]. Structures reflecting the presence of shallow intrusions, including fractures, uplifted floors, domical structures and volcanic deposits are often located within impact craters [52, 16, 49, 58]. This is particularly true in the Highlands where traces of magmatic activities are much more sparse than in the Lowlands, probably because of the larger crustal thickness [17, 19].

A class of impact craters presenting fractured, uplifted floors, as well as signs of extrusions has even been defined as floor-fractured craters (FFCs) by [49] and studied by [22]. These endogeneous modifications reflect deformation attributed to the emplacement of shallow horizontal sills or laccoliths [49, 22, 57].

The Moon is an interesting case to study the emplacement of shallow intrusions for several reasons. The lunar crust structure, thickness and density are well constrained by to the high resolution gravity data from the GRAIL mission [68]. The average lunar crust density is particularly low, such that mafic magmas

are negatively buoyant, suggesting that a mechanism different from buoyancy may drive the process of magma transport in the crust. In the Highlands, magmatic intrusions and volcanic eruptions seem preferentially located below or within impact craters where the stress state is likely affected by the presence of the crater topography itself. Craters can be seen as mass deficits unloading the underlying medium and favoring magma ascent and horizontalization at shallow depths [32, 28]. The lunar setting offers thus a unique opportunity to study the role of crustal stress field modification on magma emplacement and to compare to terrestrial volcanic settings where loads and unloads are argued to play an important role in the evolution of their plumbing system [38, 46]. FFCs in particular, provide unique extraterrestrial volcanic settings to test whether the different mechanisms proposed to influence magma transport and shallow emplacement on Earth apply elsewhere in the solar system. They also raise the question of the origin of the magma and whether it is stored at intermediate depths within the crust, at the Moho, or in the mantle.

Here we study magma ascent and emplacement in the lunar crust combining two independent quantitative observations specific to FFCs: the amount of floor uplift and the total length of floor fractures. We show first that those two quantities can be related to the overpressure leading to magma emplacement below FFCs provided that a significant part of the elastic energy of deformation are relaxed by the formation of fractures. This condition appears to be valid for a significant number of FFCs located in the Highlands or at the boundaries between the Highlands and the lunar maria.

We then study how those two observations vary as a function of crater radius and crust thickness. Since the magma overpressure in the shallow intrusion is inherited from the overpressure responsible for magma transport, we confront the two observations with a model of magma ascent within the crust. This model accounts for the unloading caused by impact craters and allows to understand how the magma can ascend in the lunar crust while being negatively buoyant [32]. Additionnally, we specify the conditions of magma storage within the lunar crust. Through those observations, the proposed model and the comparison with terrestrial volcanic systems, we discuss how buoyancy and stress induced by crater unloading play a role on magma transport and emplacement below FFCs. Finally, we suggest that the total fracture length measured at FFCs provide insights into the role of inelastic processes on magma emplacement at shallow depths in the lunar crust.

2. Two quantitative observations linked to the magma overpressure inside crater-centered intrusions

In this section, we present two independent observations pertaining to FFCs that can be related to the magma overpressure characterizing shallow crater-centered intrusions. Magma overpressure is defined as the difference between the pressure inside the magma and the local pressure acting orthogonal to the magma body wall; it induces host rock deformation, allowing magma emplacement within the crust. The overpressure in shallow intrusions is inherited from

the magma overpressure in its deep source that is responsible for magma ascent and from the subsequent intrusion emplacement below impact craters.

2.1. The total fracture length on FFCs floors

According to Griffith's theorem of brittle fracture, when failure occurs, change in the total energy of deformation is balanced by the energy required for the creation of new fractures [14, 11]. In the case of crater floor deformation caused by the spreading of an underlying magmatic intrusion, applying the Griffith's theorem consists in balancing the energy required to form the fractures observed at FFCs with variations of the elastic energy of deformation induced by the intrusion.

The appearance of new fractures consists in the creation of new surfaces that are associated with the energy

$$E_G = \Gamma L h. \tag{1}$$

The Griffith energy or fracture energy Γ is a material property generally assumed constant which corresponds to an energy per unit of surface. The energy necessary to fracture the rock is therefore proportional to the surface created, Lh, where L is the total length of fractures and h their depth.

The value of Γ varies significantly upon the mode of failure, be it tensile or shear failure. Laboratory measurements for rocks show that $\Gamma \simeq 10$–10^3 J.m^{-2} for tensile failure while $\Gamma \simeq 10^4$–10^7 J.m^{-2} for shear failure [20, 25, 61]. The value of Γ depends also on rock type and whether the rock is already damaged or not. The largest values of Γ are associated with rocks that already possess damages such as microcracks, meaning that such rocks are more difficult to break because part of the work used to deform them is dissipated by inelastic processes pertaining to those damages [20, 71].

Let's now express the energy of deformation associated with a shallow magmatic intrusion. We follow a common assumption and consider that the host rock deforms elastically [40, 57]. The elastic deformation energy density (or energy per unit of volume) scales as $\sigma\varepsilon/2$ where σ is the stress in the host rock and ε the deformation of the host rock caused by a magmatic intrusion [e.g 59].

We first consider the case where the magma makes room for itself by compressing the host rock. This is the case for sills and can be considered valid as long as the characteristic horizontal length of the intrusion is smaller or similar to its depth. The stress σ compressing the host rock scales with the sill overpressure ΔP and the deformation ε scales with $\Delta P/E$ where E is the Young modulus [53, 51]. The associated energy density of deformation is therefore proportional to $\Delta P^2/(2E)$.

The volume of the overburden deformed by the sill is proportional to $\lambda^2 T$ where λ is the characteristic horizontal size of the intrusion and T is the intrusion depth. Multiplying the energy density by the deformed volume gives the total elastic energy of deformation

$$E_S = \frac{1}{2}\frac{\Delta P^2}{E}\lambda^2 T \gamma_S \tag{2}$$

where γ_S is a dimensionless constant accounting for the sill shape and boundary conditions. Values of γ_S are not given a priori because the exact intrusion shape is not known, but its effects are later discussed.

Assuming that the entire energy of deformation of the overburden is dissipated by the creation of new fractures of total length L, we get that

$$\frac{\Delta P^2}{2E}\lambda^2 T\gamma_S = \Gamma L h \Leftrightarrow \Delta P = \sqrt{\frac{2E\Gamma hL}{\gamma_S \lambda^2 T}} \tag{3}$$

which shows that the magma overpressure is proportional to the square root of the total fracture length.

We consider now the case where the characteristic intrusion length is larger than its depth ($\lambda > T$); the intrusion bends the upper elastic layer and is called a laccolith [e.g, 40, 31]. The resulting deformation ε is proportional to the curvature radius and to the thickness of the plate $\varepsilon \sim Tw/\lambda^2$, where w is the vertical displacement, and the stress σ is proportional to ETw/λ^2 [60, 40]. Vertical displacement is proportional to the overpressure and scales with $\Delta P\lambda^4/(ET^3)$, so that the bending energy density as a function of overpressure scales with $\Delta P^2\lambda^4/(2T^4E)$. Multiplying the bending energy density by the volume of the deformed overlying plate $\sim \lambda^2 T$ gives the total elastic energy of deformation

$$E_L = \frac{\Delta P^2 \lambda^6}{2ET^3}\gamma_L \tag{4}$$

where E_L is the deformation energy associated with a laccolith and γ_L is a dimensionless constant that depends upon laccolith geometry and boundary conditions [60]. Assuming that the deformation energy is dissipated by the formation of fractures gives:

$$\Delta P = \sqrt{\frac{2T^3 ELh\Gamma}{\gamma_L \lambda^6}}. \tag{5}$$

Hence, regardless of the mode of deformation, the magma overpressure is proportional to the square root of the fracture length $\sqrt{L}$. Note that, as expected, the two scaling laws 3 and 5 are the same when $T \simeq \lambda$, *i.e.,* when the intrusion depth is approximately equal to its characteristic horizontal size. We expect therefore that, when the intrusion starts to interact with the free surface, $T \simeq \lambda$ and (3) should be considered; however, when $T < \lambda$, bending prevails and (5) has to be considered.

The coefficients γ_S and γ_L depend on the exact intrusion geometry and boundary conditions. We expect however that their effects on the expressions of ΔP (3) and (5) are of order 1. If the sill is considered as a 'penny-shaped' crack with uniform pressure distribution then $\gamma_S = 8(1-\nu^2)/3 \simeq 2.5$ [53]. For a circular laccolith that bends a plate clamped at its edge $\gamma_L \simeq 0.2$ whereas if one considers a plate with simply supported edge $\gamma_L \simeq 1.3$ (Supplementary Material Section S4).

The total fracture length L is taken to be the sum of the length of each fracture segment observed on the floors of FFCs. Equations (3) and (5) show that this quantitative observation provides information on the intrusion overpressure at emplacement depth. To estimate the total fracture length on the floor of a crater, the fracture segments on its floor were mapped manually on LROC WAC images centered on the FFC using the imageJ software. Figure 1 shows three examples of FFCs for which fractures can be observed. More information on the estimation of L is given in Supplementary Section S1.

2.2. The uplift of FFCs' floors

A common morphological characteristic of FFCs is that they are in general shallower than their pristine counterparts [49, 22]. [37] found that the depth d^{fresh} and radius R of fresh craters are related through the following empirical relationship:

$$d^{\text{fresh}} = 1.044(2R)^{0.301}, \tag{6}$$

where d^{fresh} is defined from the crater rim and d^{fresh} and R are expressed in kilometers. For FFCs, the observed depth d^{obs} is in general shallower than the depth d^{fresh} obtained using (6) and the FFC radius [22, 58].

This observation suggests that the floor of FFCs are either uplifted or filled. The uplift or filling of FFCs can therefore be estimated using the difference

$$\Delta d = d^{\text{fresh}} - d^{\text{obs}}, \tag{7}$$

where d^{obs} is the observed floor depth defined from the crater rim. When the floor elevation is asymmetrical, d^{obs} is taken as the distance between the rim and the most elevated part of the crater floor so that d^{obs} represents a minimum observed depth and Δd captures a maximum difference between d^{fresh} and d^{obs}. Further details on the estimation of d^{obs} are given in the Supplementary Section S2. For instance, for the crater Metius, which is not a FFC, we indeed find $\Delta d \simeq -0.1 \pm 0.2$ km while for FFCs Arzachel, Atlas and Haldane, Δd is respectively 1.1 ± 0.4 km, 1.9 ± 0.3 km and 2.5 ± 0.3 km (Figure 1). For FFC Haldane, the continuity in the topography and aspect of the floor in between the North-West part of the crater and the adjacent terrain suggests that Δd may represent its filling by adjacent maria (Figure 1). The location of Haldane is indicated by the black star on the Moon's map (Figure 2a). Arzachel and Atlas, however, are not located inside a mare (the location of Atlas is indicated by the grey star on the Moon's crustal map of Figure 2a) and there is also a clear topographic discontinuity between the elevation of their floors and their surroundings. For those two craters, the value Δd more likely represents an uplift of the crater floor.

When FFCs' floors are uplifted, Δd represents the maximum thickness of the underlying magmatic intrusion [67, 58]. The final thickness of an intrusion is the result of the emplacement dynamics [5, 57]. A sequence of events leading to intrusion emplacement below impact craters and the subsequent formation of FFCs is depicted in the Figures 3. If the overburden is deformed elastically, elastic stresses contribute to the pressure balance responsible for the arrest of

the emplacement process and limit intrusion thickening (Figure 3c). However, the presence of significant fractures suggests that a non-negligible part of the elastic energy is dissipated (Figure 3d). If this is indeed the case, after intrusion emplacement, the overburden has lost most of its elastic strength. In this case, the intrusion may further spread laterally in a gravity current regime until the lithostatic stress due to the crater wall prevents its lateral extension and favors vertical growth [57]. When the developpement of fractures dissociates the roof of the intrusion from the surrounding crust (Figure 3d), the intrusion further thickens vertically [40, 66]. In the final thickening stage, the intrusion overpressure is counterbalanced by its own weight and

$$\Delta P \simeq \rho_m g \Delta d \tag{8}$$

where ΔP is the overpressure, ρ_m the magma density, g the acceleration of gravity and Δd the intrusion thickness. In other words, the final weight of the intrusion is responsible for the arrest of the emplacement process. Such a consideration was first used by [12] and later, in the context of FFCs, by [66] and [22]. We believe it is valid in the context of FFCs only if significant fracturing is observed on the crater floor.

2.3. Testing the relationships between uplift, the total fracture length and magma overpressure

Based on the assumption that a significant part of the elastic energy of deformation caused by intrusions is dissipated by fracturing at FFCs we obtain that: (i) the crater-centered intrusion overpressure is proportional to the crater floor uplift (Equation 8); (ii) the intrusion overpressure is proportional to the square root of the total fracture length observed at FFCs (Equations 3 and 5). Combining (3) or (5) and (8) results in the power law

$$\Delta d \propto L^{1/2}. \tag{9}$$

We first examine the validity of this power law relationship for FFCs. Among the 155 FFCs of the database of [22], we consider 69 FFCs selected upon the criterion that their fractures are recognizable and mappable (Figure 2a). The absence of significant fractures indeed disagrees with our starting assumption that an important part of the elastic energy of deformation has been dissipated. Examples of FFCs for which the presence of fractures is not obvious are shown on Supplementary Figure S2. We have also precluded small FFCs ($R < 10$ km) because the image resolution is too low and prevents us from mapping the fractures. We do not consider FFCs located in the South Pole-Aitken basin (SPA) because of the density anomaly characterising this region compared to the Highlands, which can induce differences in volcanic activity. No selection has been made upon the different FFC classes defined by [49] and [22]. The list of FFCs not considered in this study is provided in Supplementary Section S3.

We distinguish between FFCs located in the maria (black squares on Figure 2) and FFCs located in the Highlands (grey dots on Figure 2). For FFCs located

at the limit between the Highlands and a lunar mare, we consider them as being in the Highlands except if they are filled by the adjacent mare which is the case for Haldane, Gassendi and Runge (Figure 1 and Supplementary material Figure S3). Files containing the lists of these two categories of FFCs as well as related information used in this study are provided as Supplementary material (Section S3).

For those two categories of FFCs, the total fracture length L is plotted against the uplift or filling Δd (Figure 2b) and shows two main trends. The first trend, formed by the majority of the black squares in Figure 1b, is associated with FFCs that have the largest values of Δd. The relatively high value of Δd for those FFCs reflects the fact that most of them are essentially filled by maria (Figure 2b).

The second trend, highlighted by the black solid line, has a slope $\alpha = 1/2$ in the logarithmic diagram 2b. The fact that a large number of FFCs follow this trend suggests that the power law (9) and the assumptions leading to it are appropriate. The large majority of craters on this trend are those located in the Highlands or at the limit between the Highlands and a lunar mare. For those FFCs, Δd represents floor uplift or intrusion thickness. It seems that none of the mentioned trend is associated with a specific FFC class (Supplementary Figure S5). In the following, we only consider the subset of FFCs located in the Highlands (grey dots on Figure 2).

For this subset, both the uplift Δd and the total fracture length L increase with the crater radius at first order (Figure 4). Data also shows dispersion along this trend: differences in floor uplift and fracture length exist for craters having similar sizes. For example, Azarchel and Atlas (1) have a comparable radius (48 km for Azarchel and 43 km for Atlas), but they exhibit significant differences in floor uplift and total fracture length. Both the floor uplift and fracture length are smaller for Azarchel ($\Delta d \simeq 1.1$ km and $L \simeq 99$ km) than for Atlas ($\Delta d \simeq 1.9$ km and $L \simeq 238$ km). The observed scattering can be related to variations in crustal thickness: in general, craters with a larger uplift and longer fracture length lie on a thinner crust. Conversely, craters with a smaller uplift and shorter fracture length lie on a thicker crust: on Figure 4a,b the light grey dots, representing craters on a crust thicker than the average, form the lower part of the trend. The observed correlation between uplift and total fracture length and the dependence of those two observations with respect to crust thickness suggest that, for craters of similar size, a larger magma overpressure is associated with a thinner crust.

3. Magma ascent and emplacement induced by impact craters

3.1. The magma overpressure driving transport and emplacement

We propose to confront the quantitative observations presented in Section 2 with a model considering magma transport induced by crater unloading that builds upon the work of [32]. Such a model is attractive for several reasons: on the one hand it accounts for magma ascent towards the surface despite its negative buoyancy while explaining the fact that magmatic activity on the Moon

—be it intrusive or extrusive— is often related to impact craters. On the other hand, it allows to draw a parallel with situations on Earth where loads and unloads are argued to influence magma ascent and trajectory and on the construction of the volcanic plumbing systems [27, 46].

Dyke propagation is driven by rock deformation that results from the interplay between magma buoyancy, elastic stresses in the crust, fracture processes at the tip and viscous flow, [see 45, and references therein]. Here, we follow a common approach that consists in neglecting the rock strength. Hence, buoyancy and elastic stresses are the most important contributors to the magma overpressure at the dyke tip [23]. Although pressure drop caused by viscous flow plays an important role in the dynamics of dyke propagation, here we assume situations where the magma is static; no flow is inducing viscous resistance. We evaluate the pressure balance at the tip to test whether or not a dyke can propagate any further or stop. When the conditions at the tip are met for a dyke to propagate, we assume that viscous resistance in the tail does not prevent its propagation and the dyke can always reach a new static equilibrium where we can evaluate the pressure balance without considering viscous resistance.

To understand the effect of crater unloading on magma transport, we first need to specify the state of equilibrium of a vertical dyke that overshoots the Moon's Moho in a medium with an arbitrary stress field (Figure 3a). This set up is consistent with the dynamics of dyke propagation through a layer of lower density [56] and is commonly considered as the state of magma storage within the lunar crust [21].

The density of the magma ρ_m is larger than that of the surrounding crust ($\rho_c < \rho_m$). The vertical axis is oriented positively upward and its origin is located at the base of the crust of thickness D.

For a vertical dyke at equilibrium overshooting the Moho, the overpressure responsible for dyke opening is

$$\Delta P(z) = P_m(z) - \sigma_\perp(z) \tag{10}$$

where $\sigma_\perp$ is the stress exerted by the surrounding medium and acting normal to the dyke walls. The overpressure ΔP is the part of the magma pressure that causes the deformation resulting in the opening of the fissure filled with magma. Equation (10) results from the continuity of traction between the internal stress (the magma pressure) and the external stress acting along the dyke wall [65, 38].

In static conditions, the magma pressure inside the dyke is hydrostatic. The fluid pressure is expressed with respect to the lithostatic pressure at the Moho. It is therefore taken as the sum of the fluid pressure at the mantle-crust boundary $P_m(0)$ minus the weight of the overlying magma column:

$$P_m(z) = P_m(0) - \rho_m g z. \tag{11}$$

The fluid pressure at the mantle/crust boundary is the sum of the external stress acting normal to the dyke wall and compressing the fluid and an overpressure ΔP_s:

$$P_m(0) = \sigma_\perp(0) + \Delta P_s \tag{12}$$

The fluid pressure $P_m(0)$ at the base of the crust results from the fluid pressure provided by the mantle source in the mantle and its transport within the mantle.

Having specified the fluid pressure contributing to (10), we can provide an expression for the overpressure:

$$\Delta P(z) = [\Delta P_s + \sigma_\perp(0) - \rho_m g z] - \sigma_\perp(z) \tag{13}$$

We now need to specify the external stress acting normal to the dyke wall $\sigma_\perp(z)$ which pertains to the crustal stress state.

3.2. The overpressure opening a dyke in a lithostatic stress field

We are interested in the effect of a crater unloading on the overpressure ΔP associated with a vertical dyke and expressed in Equation (13). Let's assume that the state of stress in the crust is initially lithostatic, hence $\sigma_\perp(z) = \rho_c g(D - z)$ and $\sigma_\perp(0) = \rho_c g D$. In this case, the overpressure expresses:

$$\Delta P(z) = \Delta P_s + \Delta\rho g z, \tag{14}$$

where $\Delta\rho = \rho_c - \rho_m < 0$ is the density contrast between the crust and magma. Equation (14) shows that the terms contributing to the driving pressure are the source overpressure and the buoyancy term $\Delta\rho g z$ [65]. Because, in the lunar crust, the magma is negatively buoyant, the driving pressure $\Delta P(z)$ becomes null when $(\rho_m - \rho_c) g z = \Delta P_s$, *i.e.,* when the initial fluid overpressure ΔP_s is balanced out by the negative buoyancy of the magma. When the overpressure is null, the magma pressure cannot counteract the surrounding stresses acting on the fissure filled with magma; it closes at $z = L_{os}$ and cannot propagate any further [65, 38]. Hence, if a vertical dyke overshoots the lunar crust-mantle boundary by a length L_{os}, then L_{os} is such that:

$$\Delta P(L_{os}) = \Delta P_s + \Delta\rho g L_{os} = 0. \tag{15}$$

The length L_{os} corresponds to the maximum length that the vertical dyke can reach in a negatively buoyant crust, in absence of a crater. In the case where L_{os} is significantly smaller than the crustal thickness, the magma cannot reach a shallow depth and form a shallow intrusion. In the following, we treat L_{os} as a convenient parameter reflecting the overpressure that the dyke has acquired from its source and its positive buoyancy in the mantle. External regional stresses, such as tensile stresses produced by mare loads, might also contribute to L_{os} [33].

3.3. The overpressure opening a dyke in a stress field modified by crater unloading

We now consider the effect of a crater which consists in a surface mass deficit that modifies the crustal state of stress [32]. On Earth, in volcanic settings, a similar situation occurs after partial destruction of a volcanic edifice [39, 26].

The stress perturbation caused by a crater is modeled as a thin cylindrical unloading of radius R and depth d^{fresh} over an elastic half-space, where R and

d^{fresh} are related through (6) [54, 32]. A half-space model is appropriate here because most of the studied craters have a radius smaller than the lithosphere elastic thickness that is between 70 km and 100 km [see Supplementary Figure S4c, and 32]. The stress components of the perturbation of the lithostatic stress field at the crater axis are given by:

$$\begin{cases} \Delta\sigma_{rr} = \Delta\sigma_{\theta\theta} = -\dfrac{1}{2}\rho_c g d^{\text{fresh}} R \left[-\dfrac{(D-z)R}{(R^2+(D-z)^2)^{\frac{3}{2}}} + \dfrac{1+2\nu}{R} - \dfrac{(1+2\nu)(D-z)}{R(R^2+(D-z)^2)^{\frac{1}{2}}} \right] \\ \Delta\sigma_{zz} = -\rho_c g d^{\text{fresh}} R \left[\dfrac{1}{R} - \dfrac{(D-z)}{R(R^2+(D-z)^2)^{1/2}} + \dfrac{(D-z)R}{(R^2+(D-z)^2)^{3/2}} \right]; \end{cases} \tag{16}$$

[54, 38]. The components $\Delta\sigma_{rr}$, $\Delta\sigma_{\theta\theta}$ and $\Delta\sigma_{zz}$ are respectively the radial, tangential and vertical stress perturbations induced by the unload. Those perturbations —made dimensionless by dividing by the characteristic pressure $\rho_c g d^{\text{fresh}}$— are plotted in Figure 5 as a function of dimensionless depth $(D-z)/R$.

Because the perturbated stress field is anisotropic, stresses acting on the dyke walls depend on the orientation of the magma-filled fissure. For a vertically oriented dyke, as assumed in Section 3.1, centered at the crater axis, the component of the stress perturbation normal to the dyke wall is the horizontal stress $\Delta\sigma_{rr} = \Delta\sigma_{\theta\theta}$ (Figure 3b).

Adding this perturbation to the new expression for $\sigma_\perp$ in (13) gives

$$\Delta P(z) = \Delta P_s + \Delta\rho g z - \Delta\sigma_{rr}(z). \tag{17}$$

Note that we assume that the fluid pressure at the Moho remains unchanged by the stress perturbations caused by unloading despite the fact that the surrounding stress has changed. This would be valid in particular when the fluid is pressurized by a deeper source that is not affected by the modification of the stress field caused by the crater [32]. It implies that the elastic stress caused by crater unloading and acting on the dyke at the Moho level is relaxed by the source fluid pressure.

It is convenient to express $\Delta P(z)$ as a function of the maximum overshoot length L_{os} that the dyke would reach in the crust in a lithostatic stress state. Using (15) in (17) we obtain:

$$\Delta P(z) = (\rho_c - \rho_m) g (z - L_{os}) - \Delta\sigma_{rr}(z). \tag{18}$$

Because the stress perturbation induced by the unload is mainly extensive ($\Delta\sigma_{rr} < 0$; Figure 5), Equation (18) shows that the presence of the crater acts to reduce the stress exerted by the host rock on the dyke walls. Contrary to the case where the external stress is lithostatic, the overpressure $\Delta P(L_{os})$ can become strictly positive and the dyke is able to open and further propagate towards the surface.

Note that the framework described above can apply to two distinct scenarios. In the first case, a vertical dyke first overshoots the Moho and propagates in a crust in a lithostatic state until it reaches the equilibrium length L_{os} defined by (15). Impact cratering occurs in a second step, modifying the stress field

and allowing further dyke propagation. In the second case, impact cratering occurs first and the magma rises through a crustal stress field pre-modified by the crater unloading. While in the latter scenario the dynamics of impact cratering itself does not come into play, the former implies that the transient effects associated with impact cratering (such as the transient cavity and shock waves propagation) do not permanently modify the pre-existing dyke system overshooting the Moho. This is valid for small enough craters such that $R \gtrsim$ 50 km since the ratio between the transient cavity depth and the crater radius is $\simeq 1:2$ [29] and the amplitude of the shock wave attenuates rapidly with depth [8]. For large craters ($R \lesssim 50$ km and more) this assumption does not apply since the transient cavity depth is then similar or larger than the crust thickness itself.

4. Results: overpressure at emplacement depth

In order to confront the proposed model to the quantitative observations presented in Section 2, we need to evaluate the magma overpressure in the shallow intrusion that led to floor uplift and fracture formation. At intrusion depth T, the distance from the Moho is $z = D - T$ and the flow transitions to horizontal (Figure 3c). The vertical stress component applying on the wall of the sill is dissipated by the formation of fractures in the roof while the horizontal stress component at the tip of vertical dyke maintains the dyke open, allowing the feeding of the horizontal intrusion (Figure 3d). The overpressure that allows the feeding of the intrusion thus expresses :

$$\Delta P(D-T) = (\rho_c - \rho_m) g (D - T - L_{os}) - \Delta\sigma_{rr}(D-T). \tag{19}$$

The overpressure mainly depends on $\Delta\sigma_{rr}$ that varies with the crater radius R, the density contrast between the crust and magma $\Delta\rho$, the thickness of the crust D, the intrusion depth T and the height above the mantle-crust boundary, L_{os}, reached by the dyke in absence of crater. Note that the only value that depends on crater size is the radial stress perturbation at emplacement depth.

For simplicity and as the intrusion is shallow and both $D \gg T$ and $R \gg T$ [58], we estimate $\Delta\sigma_{rr}$ at emplacement depth from its surface value $\Delta\sigma_{rr}(D) = -0.5(1+2\nu)$ (Equation 16), which gives $\Delta\sigma_{rr}(D) = -0.75$ for $\nu = 0.25$ (Figure 6.

We compare the modeled overpressure with the intrusion overpressure estimated from the uplift (Figure 6). We use $g = 1.62$ m.s^{-2}. The crust density is assumed constant and is taken equal to $\rho_m = 2550$ kg.m^{-3} *i.e.,* the average density of the lunar crust in the Highlands as inferred from gravity data [68]. For the set of studied craters (grey dots in Figure 2), the crustal thickness D ranges from $\simeq 20$ km to $\simeq 45$ km and the median is $\simeq 33$ km (Figures 2a and 4).

The two other parameters $[\Delta\rho, L_{os}]$ are varied and we look for the set of parameters for which the modeled overpressure values of overpressure best compare with estimated ones. When the density contrast is low, the term associated with the stress perturbation caused by crater unloading dominates in

(19). In this case, the buoyancy term does not have a significant influence and the overpressure varies mostly with crater radius and not significantly with the crustal thickness D or the overshoot in absence of a crater L_{os} (see results for $\Delta\rho/\rho_c = -0.02$ in Figure 6a,b).

As the density contrast between the crust and magma becomes more influential, the crustal thickness as well as L_{os} have more impact on the overpressure value (Figure 6c,d,e,f for $\Delta\rho/\rho_c = [-0.06, -0.10]$). As $\Delta\rho/\rho_c$ increases, the difference in overpressure values between two solid lines (corresponding to two crustal thicknesses) increases. For example, for $\Delta\rho/\rho_m = -0.06$, the calculated overpressure value decreases by $\simeq 5$ MPa if the crustal thickness increases by 15 km while it only decreases by $\simeq 1$ MPa for $\Delta\rho/\rho_c = -0.02$.

One set of parameters —$[\Delta\rho/\rho_c, L_{os}] = [-0.1, 15$ km]— appears to well explain the estimated overpressure at emplacement depth below FFCs and its variability with R and D (Figure 6c). The associated value of $\Delta\rho/\rho_c$ (-0.1) corresponds respectively to $\rho_m \simeq 2800$ kg.m^{-3} for $\rho_c \simeq 2550$ kg.m^{-3} which is consistent with values used for lunar magma density although in the lower range [69, 32]. A tradeoff exists between the value of the buoyancy and the value of the overshoot in absence of a crater L_{os}. For example, a lower density contrast together with a smaller overshoot such as $[\Delta\rho/\rho_c, L_{os}] = [-0.06, 10$ km] can produce results that also fit the data.

In any case, it seems that the overshoot length, L_{os}, needs to be large enough in order for our modeled overpressure to fit the estimated one (Figure 6). Interestingly, our model constrains the value of L_{os} and shows that dykes in the lunar crust may reach spontaneously $\simeq 15$ km above the Moho if no external stress due to a crater is applied to the dyke wall. As explained in Section 3.2, this overshoot reflects the overpressure a dyke can acquire in the mantle but also possibly because of existing external regional stress that can also act on the dyke walls. The value of L_{os} required to fit our data is also consistent with the fact that, in the Lowlands, where the crustal thickness is lower, magmatic activity is much frequent than in the Highlands simply because the magma can reach the surface without necessitating the contribution of external tensile stress [17]. In section 5.1 we also discuss how L_{os} influences the magma trajectory.

5. Discussion

5.1. Overshoot of the dyke and magma trajectory

We have shown that an unloading associated with an impact crater can modify the overpressure of a vertical dyke emanating from the mantle-crust boundary favoring its ascent towards the surface. Loads and unloads also induce specific orientations of the principal stresses which can act upon the dyke trajectory that tends to align in the direction of maximum compressive stress [64, 30].

In the context of FFCs, [33] have shown that a vertical dyke emanating from the mantle-crust boundary and affected by crater unloading will tend to become horizontal because the maximum compressive stress induced by the

crater is horizontal at its axis and sub-horizontal between the crater axis and the crater wall. Indeed, the straight vertical trajectory of the dyke is unstable and any small deviation of the dyke from the vertical axis necessarily grows [7]. Such a deviation from the vertical trajectory can prevent magma ascent and emplacement at shallow depths below impact craters. [33] suggest that the additional overpressure provided by tensile stress caused by mare loads prevents the deep horizontalization of the dyke below the impact crater and, in some case, is necessary to explain magma emplacement at shallow depths. Following this line of thought, we show below that, regardless its source, a magma overpressure that allows the dyke to reach a large enough overshoot L_{os} in absence of a crater is necessary to prevent deep horizontalization of the magma below the impact crater.

In a situation where unloading occurs, the ability of the dyke to ascend first and then spread at shallow depths depends on the rate at which a vertical dyke deviates from its initial direction to align with σ_1. If the rate of deviation is high, the dyke turns rapidly at large depths. Conversely if the deviation rate is low, the dyke propagates vertically before deviating and can therefore reach a shallow depth. The deviation rate from the straight vertical trajectory depends on the difference between the maximum compressive stress and the stress acting on the dyke walls ($\Delta\sigma_1 - \Delta\sigma_\perp$) as well as on the stress intensity factor at the crack tip K [7, 30]. The stress intensity factor K varies with $\Delta P\sqrt{L^*}$ where L^* is a length characterizing the dyke and ΔP is the overpressure at the dyke tip. The theoretical results of [7] demonstrate that the characteristic distance λ_v over which the dyke turns to align with σ_1 is proportional to $K^2/(\sigma_1 - \sigma_\perp)^2$: the larger the stress difference $\sigma_1 - \sigma_\perp$ and the smaller K, the lower λ_v is. Conversely, the larger the stress intensity factor K, the larger the value of λ_v is. This is confirmed by experimental setups meant to constitute analogues of volcanic systems [30, 28].

If a dyke overshoots the Moho and maintains its verticality before interacting with the stress field induced by crater unloading, its overshoot is mainly controlled by the overpressure that it has aquired during its ascent in the mantle and eventually by additional regional stress field so that its length is at least equal to L_{os}. When reaching the overshoot length L_{os}, the overpressure at the crack tip is simply $\Delta P(L_{os}) = -\Delta\sigma_{rr}(L_{os})$ (18). The stress intensity factor K is therefore proportional to $-\Delta\sigma_{rr}(L_{os})\sqrt{L_{os}}$ which shows that the initial dyke overshoot plays a role in the capacity of the dyke to propagate vertically towards the surface. The overshoot L_{os} should be large enough to counterbalance the forces deviating the dyke from its vertical trajectory towards the surface. This is also demonstrated experimentally by [30].

At the axis, the stress difference competing with the stress intensity factor is $\Delta\sigma_{rr} - \Delta\sigma_{zz}$. The absolute value of the stress difference increases when the dimensionless depth decreases and reaches a maximum value just below the depth $(D - z)/R \simeq 0.5$ (Figure 7); then, above, it decreases quasi linearly towards the surface. The absolute value of the horizontal stress σ_{rr} progressively increases as the dimensionless depth decreases.

At depths larger than $(D - z)/R \simeq 0.5$, it is clear that the stresses acting

to deviate the dyke from the vertical trajectory —$\Delta\sigma_{zz} - \Delta\sigma_{rr}$— dominates over the stresses that would favor propagation towards the surface $\Delta\sigma_{rr}$ (Figure 7). As a consequence, the ratio $\sigma_{rr}^2/(\sigma_{zz} - \sigma_{rr})^2$, that is proportional to the characteristic length over which the dyke turns to align with σ_1 [7], is significantly different from 0 for dimensionless depths $(D - z)/R \leq 0.5$. It means that if the tip of the dyke is initially located at a shallower depth than $\simeq 0.5R$, it is more likely to propagate vertically and emplace at shallow depths below impact craters. This is even more true because, above the dimensionless depth $(D - z)/R \simeq 0.5$, the stress difference $\Delta\sigma_{zz} - \Delta\sigma_{rr}$, that acts to the dyke tip decreases as it approaches the surface.

Let's consider a crater of radius $R \simeq 40$ km located on a crust of thickness $D \simeq 30$ km. In this case, the dyke horizontalises at shallow depths only if its tip is initially above the depth $(D - z) \simeq 0.5R \simeq 20$ km which means that the dyke overshoot needs to be at least $\simeq 10$ km.

Both the facts that the stress intensity factor, and that the ratio $\sigma_{rr}^2/(\sigma_{zz} - \sigma_{rr})^2$ is significantly different from 0 at depths smaller than $\simeq 0.5R$, imply that the length of the overshoot L_{os} should be significant in order to ensure dyke propagation towards the surface and spreading at a shallow depth. Results shown on Figure 6f for $\Delta\rho/\rho_c = -0.1$ also favours a value of $L_{os} \simeq 15$ km. Taken altogether, this would suggest that dykes emanating from the mantle-crust boundary overshoot significantly the Moho if no external stress induced by craters load is present.

5.2. Deformation mode of FFCs from the total fracture length

The total fracture length offers the opportunity to mine for further information on magma emplacement and on the process of fracturing in general. For instance it enables to clarify how the scaling of the fracture length with respect to other parameters might depend on the mode of deformation of the host rock. While, on Earth, the dimensions of exposed dykes and sills are exploited to extract information on their mechanisms of emplacement [3], the length of fractures at FFCs is an observation that has not been exploited so far. It is an attractive perspective since floor-fractured craters are present on other planetary bodies [50, 66]. Mars, in particular, seems to host a significant amount of FFCs, the formation of which is still under debate [48, 2].

In order to understand the information contained in the total fracture length, we exploit the correlation between the uplift Δd and the square root of the total fracture length $\sqrt{L}$ obtained for craters in the Highlands (Figure 8). The linear regression line that fits the set of data points on Figure 8 has a slope $a \simeq 4$ m$^{1/2}$.

This slope can be expressed from the coefficient that relates floor uplift to the square root of the fracture length estimated. Combining Equations (3) or (5) with (8) gives that for a sill

$$\Delta d = \left[\frac{1}{\rho_m g} \sqrt{\frac{2E\Gamma h}{\lambda^2 T \gamma_S}} \right] \sqrt{L} \tag{20}$$

while for a laccolith

$$\Delta d = \left[\frac{1}{\rho_m g}\sqrt{\frac{2T^3 E\Gamma h}{\lambda^6 \gamma_L}}\right]\sqrt{L}. \tag{21}$$

The relations (20) and (21) provide two theoretical expressions for the coefficient relating the uplift of the crater floor to the square root of the total length of fractures:

$$\begin{cases} a_{\text{sill}} = \left[\dfrac{1}{\rho_m g}\sqrt{\dfrac{2E\Gamma h}{\lambda^2 T \gamma_S}}\right] \\ a_{\text{lacc}} = \left[\dfrac{1}{\rho_m g}\sqrt{\dfrac{2T^3 E\Gamma h}{\lambda^6 \gamma_L}}\right] \end{cases} \tag{22}$$

The comparison of the value of a derived from observations with those of a_{sill} and a_{lacc} obtained using relevant values for the different parameters can provide a simple framework to understand the process of fracture formation on lunar FFCs. The exact theoretical values of a_{sill} and a_{lacc} depend on the value of γ_S and γ_L that themselves depend on the unknown geometry of the intrusion. However both γ_S and γ_L should have an effect of order 1 on the values of a_{sill} and a_{lacc} (Section 2.1) and we will assume in the following that $\gamma_S = \gamma_L \simeq 1$.

Since magma seems to reach the surface through some of the observed fractures [9], we assume that the fracture depth h is approximately equal to the intrusion depth T ($h \simeq T$), which gives

$$\begin{cases} a_{\text{sill}} = \left[\dfrac{1}{\rho_m g}\sqrt{\dfrac{2E\Gamma}{\lambda^2 \gamma_S}}\right] \\ a_{\text{lacc}} = \left[\dfrac{1}{\rho_m g}\sqrt{\dfrac{2T^4 E\Gamma}{\lambda^6 \gamma_L}}\right] \end{cases} \tag{23}$$

The characteristic size of the intrusion λ can vary from a few hundreds of meters to tens of kilometers. For example, [66] assumed that the radius of the intrusion below the crater Taruntius is approximately 15 km. Here, we use $\lambda \simeq 10$ km in particular because fractures generally cover a surface of the crater floor of one to several 10^2 km^2 (Figure 1).

An order of magnitude for the minimum value of the intrusion depth T is $\simeq 1$ km whereas its maximum value is λ. For values of T larger than λ, the intrusion would not interact with the free surface and no fractures would be visible. As mentioned in Section 2, the mode of deformation that we associate to a sill prevails when $T \simeq \lambda$ and in this case $a_{\text{sill}} \simeq a_{\text{lacc}}$. Bending would dominate when $T < \lambda$ and in this case we use $T \simeq 1$ km. Finally we assume that $E \simeq 10^{10}$ Pa.

Because the fracture energy values span a large range of orders of magnitude depending on rock properties and rupture modes, we choose the approach of deducing Γ from a and its theoretical expressions (23). Posing $a = a_{\text{sill}}$ or

$a = a_{\text{lacc}}$, we obtain respectively

$$\begin{cases} \Gamma_{\text{sill}} = \dfrac{(a\rho_m g)^2 \lambda^2 \gamma_S}{2E} \\ \Gamma_{\text{lacc}} = \dfrac{(a\rho_m g)^2 \lambda^6 \gamma_L}{2T^4 E} \end{cases} \tag{24}$$

Using parameter values listed above, we find that $\Gamma_{\text{sill}} \simeq 10^6$ J.m^{-2} and $\Gamma_{\text{lacc}} \simeq 10^{10}$ J.m^{-2}.

Rock experiments show that when fractures occur through tensile failure of the rock samples, values for the fracture energy lies between 10 and 10^3 J.m^{-2} and are therefore several orders of magnitude lower than the ones deduced from (24) [e.g, 20, 1]. The fracture energies for shear failure, derived from experimental data and the study of natural faults systems, are larger, spanning the range between $10^4 - 10^7$ J.m^{-2} [25, 43, 61]. The value obtained for $\Gamma_{\text{sill}} \simeq 10^6$ J.m^{-2} lies well within this range of values which suggests that part of the fractures are produced by shear rupture of the host rock.

The presence of fractures produced by shear failure at FFCs can be understood by the fact that the observed uplift of the floor might be accommodated by vertical faults so that observed offsets in FFCs topographic profiles delimited by fractures may be the result of fractures produced by shear failure. Such an offset can be observed, for example, on Arzachel floor where the East fracture delimits an offset in floor elevation visible on the profile displayed on Figure 1. Alternatively, since on Earth the host rocks surrounding well exposed sills can show signs of shear failure, observed open fractures on FFCs floors may be connected to shear fractures at depth [47, 10, 55, 41]. Analog experiments of intrusion emplacement have also revealed the possibility for the presence of shear failure in the host rocks [42]. The value we obtained for Γ_{sill} is thus consistent provided that part of the fractures at FFCs are formed by shear rupture of the host rock.

The relatively large value of Γ can also be related to the highly porous and damaged state of the lunar crust [68, 13]. Experimental measurements on rocks show indeed that pre-fractured samples display fracture energies that can be an order of magnitude larger than those of intact samples [71]. In this case, the larger fracture energies account also for inelastic processes pertaining to the pre-existing damages [36, 35]. The size of the sytem may also play a role because fracture energies derived from earthquakes studies ($\simeq 10^6$J.m^{-2}) tend to be larger than those derived from rock experiments ($\simeq 10^4$J.m^{-2}) [71].

The value for $\Gamma_{\text{lacc}} \simeq 10^{10}$ J.m^{-2} —obtained for an intrusion depth T significantly smaller than its characteristic horizontal size λ— is however larger than common estimations of the shear fracture energy. In other words, if the fractures were caused by bending associated with a laccolith that extends over a distance much larger than its depth, we would expect larger values for L than what is observed. This may suggest that the fractures start to form before or when the sill starts to interact with the free surface *i.e.,* when $\lambda \leq T$. As the intrusion extends, elastic energy is dissipated by further fracture formation, limiting elastic bending of the overlying layer and allowing the intrusion to thicken and to

uplift the crater floor. If the above reasoning is correct, fracture formation is an efficient sink of elastic energy for the set of selected floor-fractured craters, that might be important to account for when modeling magma emplacement and the resulting shape of the overlying surface topography.

The reader should keep in mind that because of limited image resolution and also the possibility that fractures may exist at depth without being visible at the surface, the measured total fracture length corresponds to a lower bound of the effective total fracture length. Also, to simplify the scaling laws, we made the assumption that the fracture depth is constant and equals the intrusions depth. While those limitations affect our estimations of the elastic energy dissipated by failure, they should not affect much the order of magnitude of the estimated fracture energies Γ_S and Γ_L: increasing or decreasing L by a factor 10 modifies Γ_S and Γ_L only by a factor $\sqrt{10}$.

5.3. Deformation mode of FFCs from observed fracture patterns

The information extracted above from the study of the total fracture length at FFCs can be related to the observed fracture patterns. Classical models of elastic bending caused by shallow intrusions predict tangential stresses larger than radial stresses and therefore the formation of radial fractures [40, 62]. However, in our selected set of craters, only two craters Humbolt and Petavius, have fractures with clear radial orientations. Even for craters displaying clear domical uplift such as Nernst, Mersenius and Gauss, no clear radial fractures are observed. Most craters display instead either circumferential fractures and, even more frequently, fractures with neither clear radial nor tangential directions.

The shape of the uplift caused by elastic bending and therefore the relative amplitude of radial and tangential stresses can vary upon boundary conditions and characteristics of the encasing medium. For example, models of elastic bending that account for the crater topography can produce comparable radial and tangential stresses or even radial stresses larger than tangential stresses because of the thickening of the overlying plate towards the crater wall (Figure B1 in [57]). This explains the more frequent occurence of concentric fracture patterns than radial ones.

The majority of the observed fracture pattern are hierarchical. A hierarchical fracture pattern refers to fractures perpendicular to each others [4, 11]. Examples of FFCs with such a pattern are shown in the Supplementary Figure S6. This pattern reflects the time delay between the occurrence of the different fracture segments. Once failure occurs, the stress is relaxed in the direction perpendicular to the fracture segment in such a way that the following fracture segment would appear perpendicular to the previous one. This implies a temporal hierarchy between the different fracture segments dividing the crater floors [4].

Because a hierarchical fracture pattern suggests that fractures appear one after the other following a temporal hierarchy, the fractures may occur as the intrusion is growing and before the conditions for elastic bending are met. The formation of fractures may eventually prevent bending to occur by significantly

reducing the elastic strength of the host rock. Our estimated value of the fracture energy in the laccolith case (Section 5.2) is indeed inconsistent with common estimates of Γ hence failure may occur before conditions for bending are met.

6. Conclusions

Two independent quantitative observations pertaining to FFCs can provide information about the magma overpressure inside shallow magmatic intrusions below impact craters and thus about the stress field leading to their emplacement. Those two observations are the uplift and the total fracture length on the floor of FFCs; they can be related to the overpressure causing magma emplacement below impact craters provided that a significant part of the elastic energy of deformation is dissipated by the creation of fractures. This condition seems to be met for a large set of FFCs located in the Highlands or at the borders between the Highlands and lunar maria and showing significant fracturing of their floors. FFCs filled by mare material constitute another category of FFCs where the magmatic intrusion has probably been emplaced below an already filled crater.

For FFCs in the Highlands, the observed correlation between the floor uplift and the total fracture length suggests that those observations reflect the variability of the overpressure leading to magma emplacement below impact craters. They also demonstrate that larger overpressures are generally related to craters on a thinner crusts while lower overpressures are related to craters on a thicker crust.

This feature is predicted by a model of magma ascent that builds upon the work of [32] and which considers that an impact crater produces a modification of the stress field within the crust that can promote the ascent of magma stored within dykes overshooting the mantle/crust boundary. We show that if no additional extensive stress is present within the crust, vertical dykes probably have to overshoot the Moho by about 15 km to reach shallow depths below the craters.

Finally, we have shown that the information contained in the total length of fractures covering FFCs' floors —an observation that, to our knowledge, has not been exploited yet— opens up interesting perspectives for the study of inelastic processes associated with intrusion emplacement on the Moon as well as for the study of FFCs on other planetary bodies where processes at play during FFCs formation remain uncertain.

Acknowledgement

It is a pleasure to acknowledge an anonymous reviewer for constructive and insightful comments and suggestions on an initial version of the manuscript. The authors acknowledge financial support from the IDEXLyon Project of the University of Lyon in the frame of the Programme investissements d'Avenir (ANR-16-IDEX-0005) as well as from the Région Auvergne Rhône-Alpes. V.P.

was supported by the ANR-DFG NLE 2018 MagmaPropagator project (ANR-18-CE92-0037).

Description	Symbols	Range of Values
Variables		
Distance from the Moho	z	
Magma pressure	P_m	
External stresses acting on dyke walls	$\sigma_\perp$	
Overpressure	ΔP	
Radial stress perturbation	$\Delta\sigma_{rr}$	
Vertical stress perturbation	$\Delta\sigma_{zz}$	
Crater properties		
Crater radius	R	$13 - 103$ km
Observed crater depth	d^{obs}	$0.27 - 3.74$ km
Depth of complex fresh craters	d^{fresh}	$2.78 - 4.32$ km
Crater uplift/filling	$\Delta d = d^{\text{fresh}} - d$	$0.1 - 3.5$ km
Total fracture length	L	$14 - 1028$ km
Fracture depth	h	$0.1 - 1$ km
Dyke and intrusion properties		
Magma density	ρ_m	$2800 - 3000$ kg.m^{-3}
Density contrast	$\Delta\rho$	$100 - 500$ kg.m^{-3}
Intrusion depth	T	$0.1 - 10$ km
Intrusion characteristic size	λ	$0.1 - 10$ km
Source overpressure	ΔP_s	
Overshoot	L_{os}	$0 - 15$ km
Crustal properties		
Crustal thickness	D	$20 - 50$ km
Highlands crust density	ρ_c	2550 kg.m^{-3}
Young modulus	E	10^{10} Pa
Poisson's coefficient	ν	0.25
Fracture energy	Γ	$10 - 10^7$ J.m^{-2}

Table 1: List of variables and parameters described in the main text.

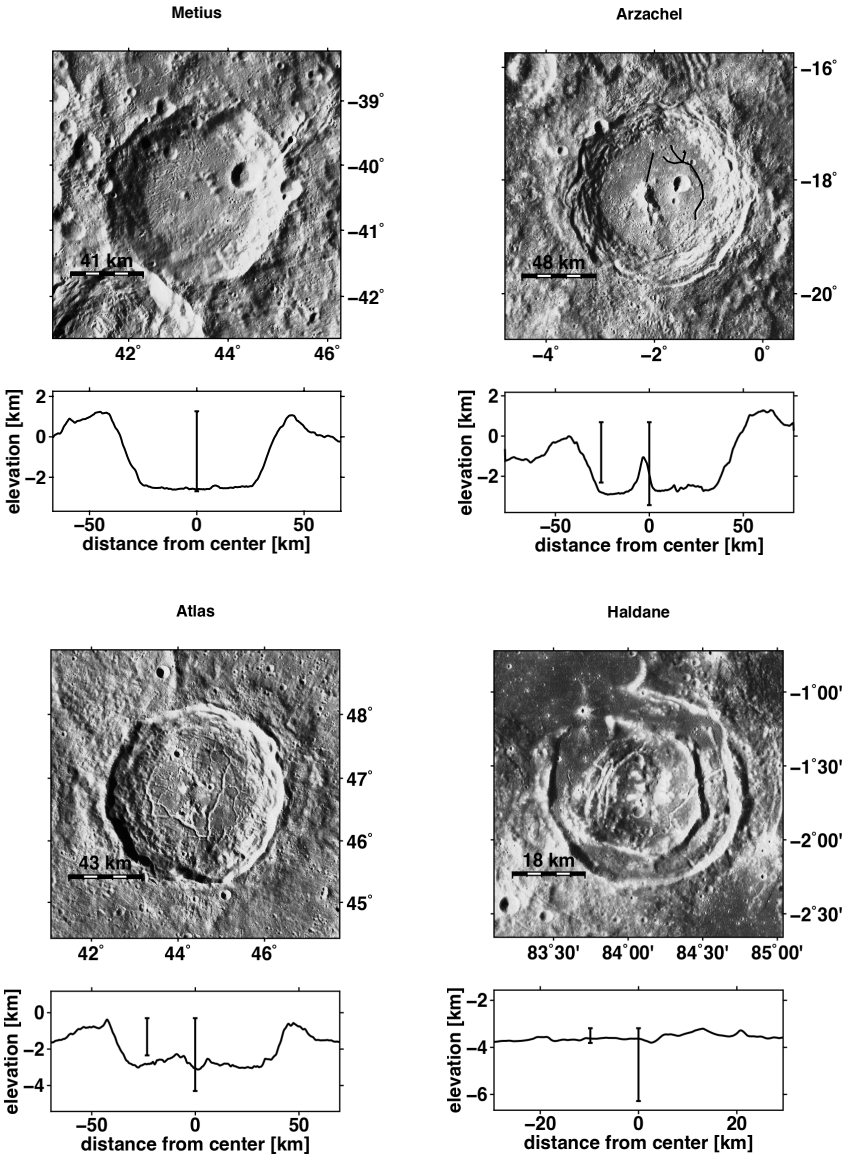

Figure 1: LROC WAC images and topographic profiles centered on four craters : Metius, Arzachel, Atlas and Haldane to illustrate the different observations used in this study. The depth indicated at the center of each profile represents d^{fresh} obtained using relation (6). The depth indicated on the left-side of each profile corresponds to the observed depth d^{obs}. The difference $\Delta d = d^{\text{fresh}} - d^{\text{obs}}$ constitutes an estimation of the uplift of the crater floor or its filling. For FFCs Arzachel, Atlas and Haldane, the fractures that cover their floors can be observed on the LROC WAS images. Examples of mapped fracture segments are represented by black lines on Arzachel LROC WAC image. For a given FFC, Δd and the total fracture length are the main observations exploited in this study.

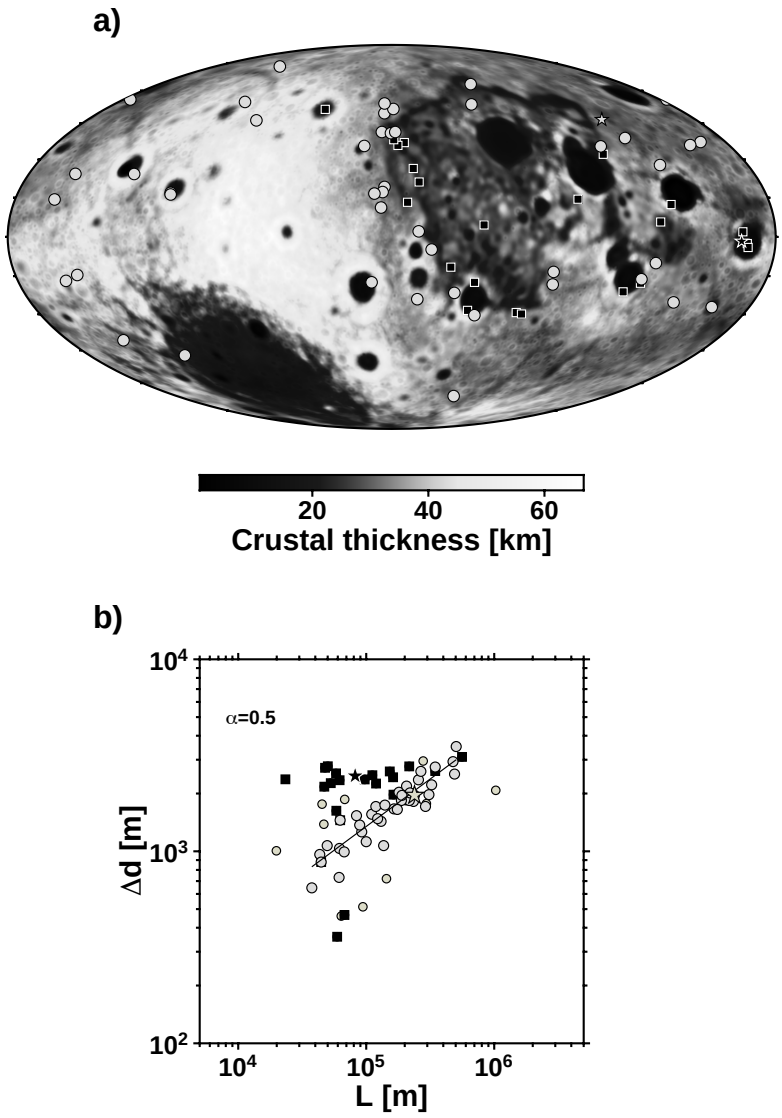

Figure 2: (a) Locations of floor-fractured craters on the crustal thickness map of the Moon. The crustal thickness map is the model 1 of [68], based on gravity data from the GRAIL NASA mission, which is the model with the lowest average thickness (34 km). The grey and black symbols show the locations of studied FFCs. Black squares represent FFCs located in the mare or at the limit between the maria and the Highlands but filled by the adjacent mare. The black star locates the crater Haldane mentioned in the main text and the grey star locates the crater Atlas. Grey dots represent FFCs located in the Highlands or at the limit between the Highlands and maria that are not filled by the adjacent mare. (b) Diagram showing FFC uplift or filling versus the total fracture length. We use the same symbols for dots as in (a).

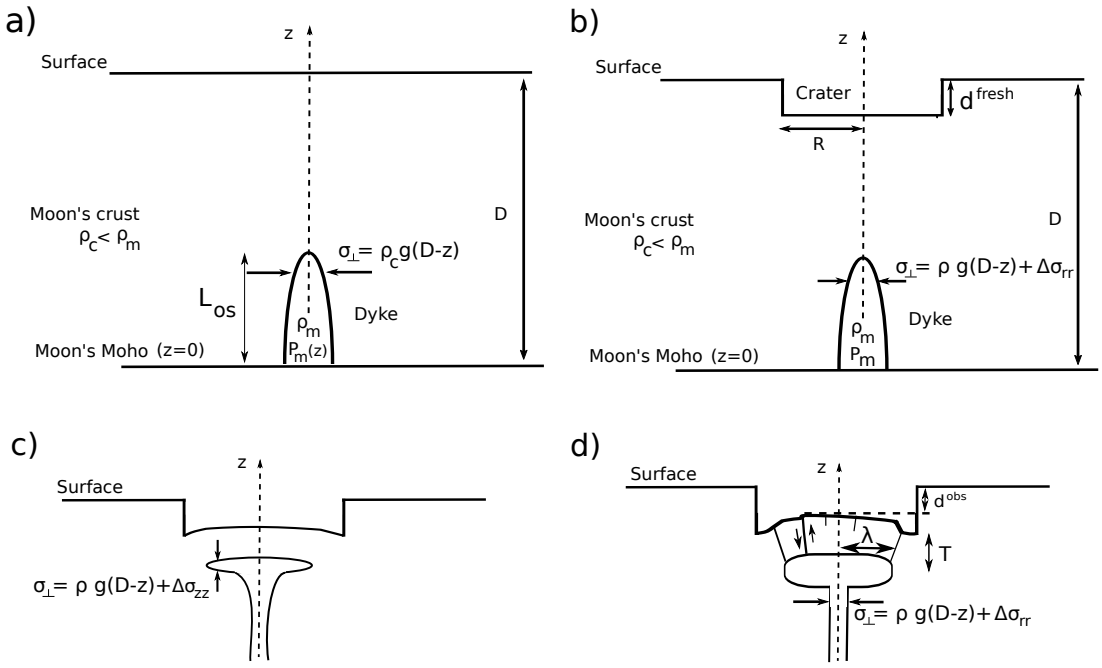

Figure 3: Schematic representation of the components of the model. a) A vertical dyke emanating from the lunar Moho is subjected to lithostatic external stresses, magma pressure is P_m and magma density ρ_m. b) After crater emplacement, the external stress exerted on the dyke is decreased by $|\Delta\sigma_{rr}|$ which is the component of the stress perturbation due to the unloading acting perpendicular to the dyke wall. c) At the intrusion depth, the magma laterally spreads. Lateral propagation is affected by the component of the stress perturbation due to the unloading acting in the vertical direction: $\Delta\sigma_{zz}$. d) Fractures relax the elastic stress acting vertically and allows the intrusion to thicken.

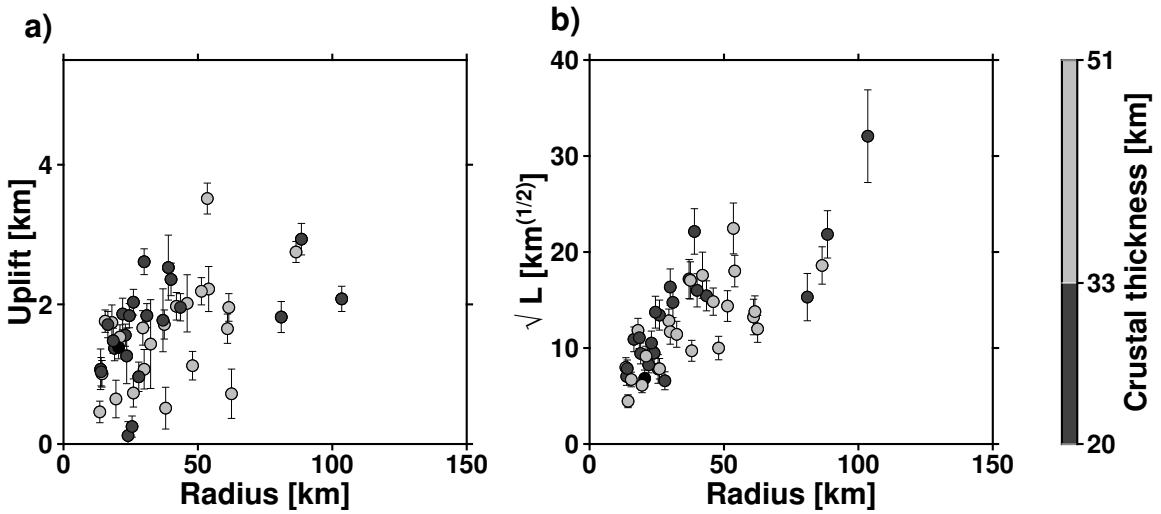

Figure 4: Two quantitative observations reflecting how the magma overpressure associated to a crater-centered intrusion varies as a function of crater radius and crustal thickness. FFCs represented here are those located in the Highlands and at the limit between the Highlands and a lunar mare (grey dots on Figure 2). a) Crater floor uplift estimated from Equation (7) versus crater radius. b) Square root of the total fracture length versus crater radius. Dark dots indicate craters located on a crust with a thickness ranging from 20 km to 33 km while dots in light gray correspond to craters located where the crust has a thickness ranging from 33 km to 51 km. The crustal thickness separating the two populations (D=33 km) corresponds to the median value of the crustal thicknesses.

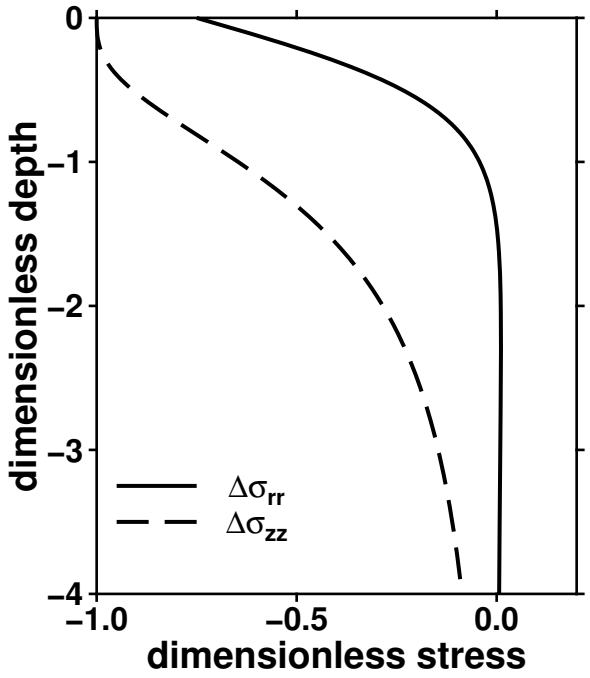

Figure 5: Variations with depth of the axial horizontal and vertical component of the stress perturbation caused by crater unloading —denoted respectively $\Delta\sigma_{rr}$ and $\Delta\sigma_{zz}$— assuming a cylindrical crater of radius R and depth d^{fresh} at the surface of an elastic half-space. The depth is made dimensionless by the crater radius R and the stress by $\rho_c g d^{\text{fresh}}$. Results were obtained using $\nu = 0.25$ and $g = 1.62$ m.s^{-2}.

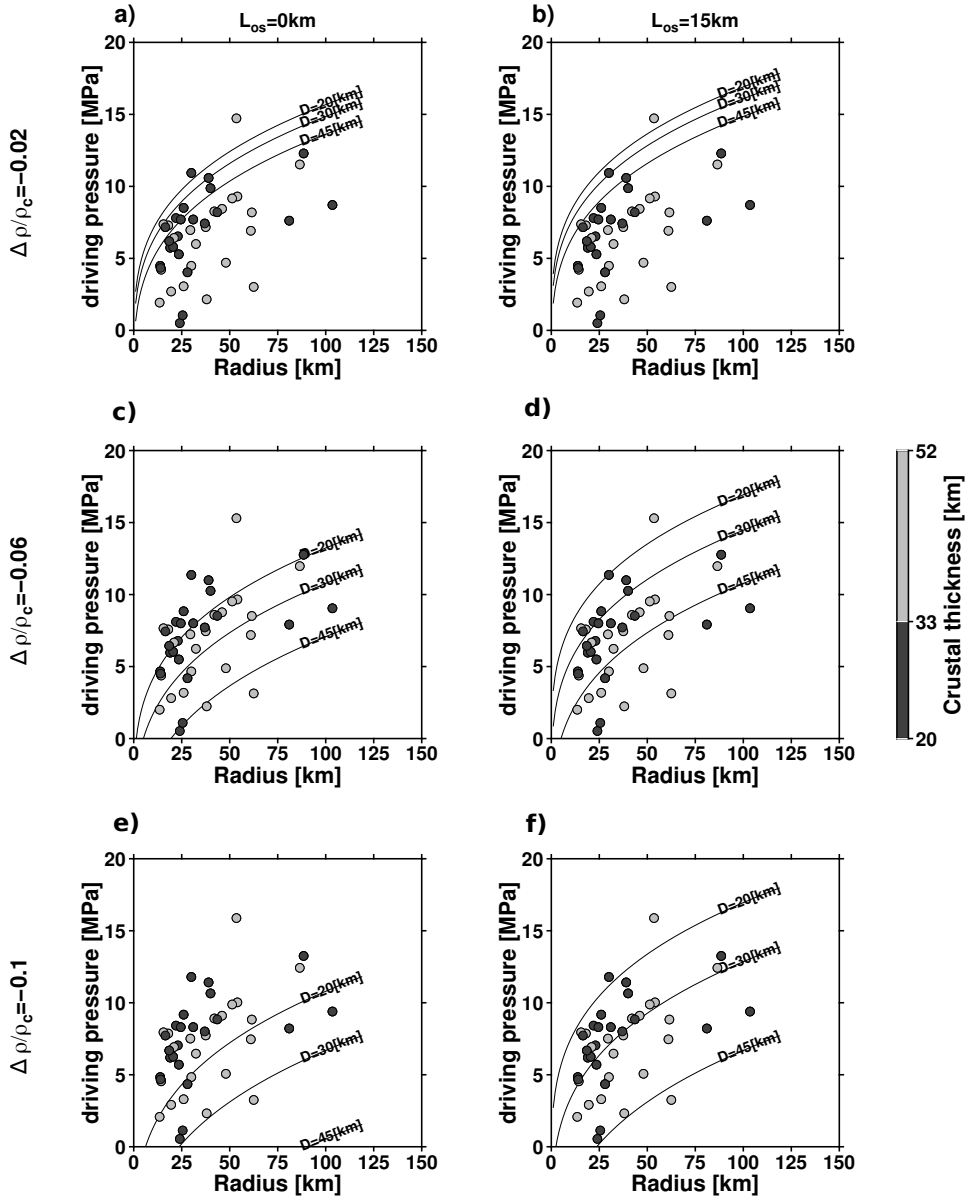

Figure 6: Comparison between the magma overpressure estimated using the uplift of crater floor and Equation (8) (dots) and the modeled overpressure from (19) (solid lines). The comparison is made for FFCs located in the Highlands or at the limit between the Highlands and lunar maria (grey dots of figure 2). Two parameters are varied: the relative buoyancy $\Delta\rho/\rho_c$ and the initial dyke overshoot L_{os}. The relative buoyancy takes values $[-0.02, -0.06, -0.1]$ and the maximum dyke overshoot in absence of a crater takes values $[0, 15]$km.

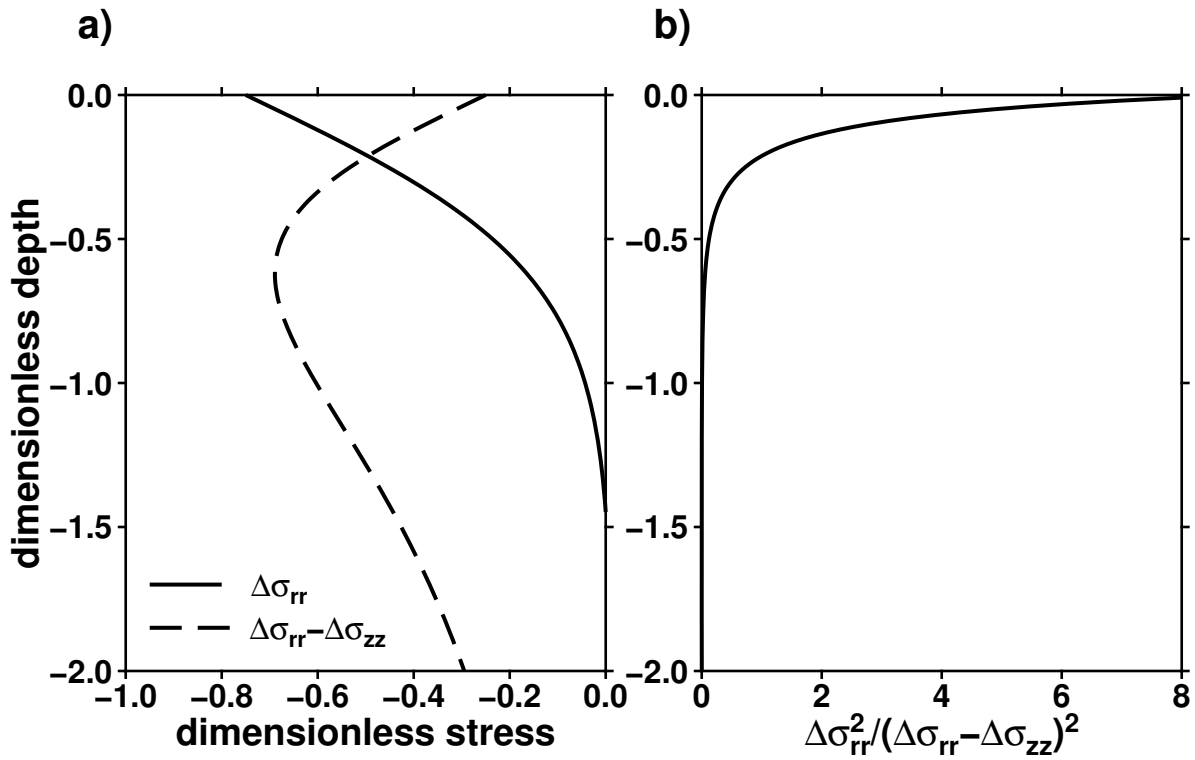

Figure 7: The different stress components affecting the trajectory of a vertical dyke in a stress field unloaded by an axi-symmetric slab. a) Variation with depth of $\Delta\sigma_{rr}$ and the difference $\Delta\sigma_{rr} - \Delta\sigma_{zz}$. Larger values of $|\Delta\sigma_{rr}|$ promote a vertical dyke trajectory while larger values of $|\Delta\sigma_{rr} - \Delta\sigma_{zz}|$ promote deviation from the vertical trajectory. b) Variation with depth of the ratio $\Delta\sigma_{rr}^2/(\Delta\sigma_{rr} - \Delta\sigma_{zz})^2$ which is proportional to the characteristic distance λ_ν over which a vertical dyke turns to align with the direction of maximum compressive stress.

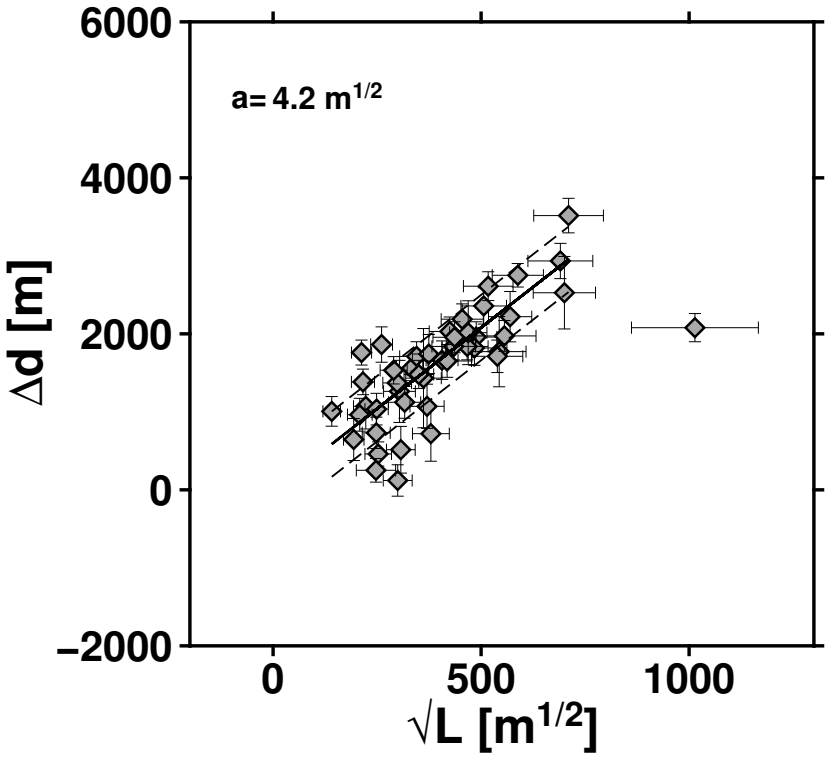

Figure 8: Crater uplift versus square root of total fracture length for craters located in the Highlands or at the limit between the Highlands and lunar maria (grey dots on figure 2). The solid line represents a linear regression fit.

References

[1] Atkinson, B. K. (1984). Subcritical crack growth in geological materials. *Journal of Geophysical Research: Solid Earth*, 89(B6):4077–4114.

[2] Bamberg, M., Jaumann, R., Asche, H., Kneissl, T., and Michael, G. (2014). Floor-Fractured Craters on Mars – Observations and Origin. *Planetary and Space Science*, 98:146–162.

[3] Becerril, L., Galindo, I., Gudmundsson, A., and Morales, J. M. (2013). Depth of origin of magma in eruptions. *Scientific reports*, 3:2762.

[4] Bohn, S., Pauchard, L., and Couder, Y. (2005). Hierarchical crack pattern as formed by successive domain divisions. *Physical Review E*, 71(4).

[5] Bunger, A. P. and Cruden, A. R. (2011). Modeling the growth of laccoliths and large mafic sills: Role of magma body forces. *Journal of Geophysical Research*, 116(B2).

[6] Coleman, D. S., Gray, W., and Glazner, A. F. (2004). Rethinking the emplacement and evolution of zoned plutons: Geochronologic evidence for incremental assembly of the Tuolumne Intrusive Suite, California. *Geology*, 32(5):433.

[7] Cotterell, B. and Rice, J. (1980). Slightly curved or kinked cracks. *International journal of fracture*, 16(2):155–169.

[8] Ferrière, L., Koeberl, C., Ivanov, B. A., and Reimold, W. U. (2008). Shock metamorphism of bosumtwi impact crater rocks, shock attenuation, and uplift formation. *Science*, 322(5908):1678–1681.

[9] Gaddis, L. R., Staid, M. I., Tyburczy, J. A., Hawke, B. R., and Petro, N. E. (2003). Compositional analyses of lunar pyroclastic deposits. page 19.

[10] Gerbault, M. (2012). Pressure conditions for shear and tensile failure around a circular magma chamber; insight from elasto-plastic modelling. *Geological Society, London, Special Publications*, 367(1):111–130.

[11] Ghabache, E., Josserand, C., and Séon, T. (2016). Frozen Impacted Drop: From Fragmentation to Hierarchical Crack Patterns. *Physical Review Letters*, 117(7).

[12] Gilbert, C. G. and Dutton, C. E. (1880). *Report on the Geology of the Henry Mountains*. US Government Printing Office.

[13] Gillet, K., Margerin, L., Calvet, M., and Monnereau, M. (2017). Scattering attenuation profile of the Moon: Implications for shallow moonquakes and the structure of the megaregolith. *Physics of the Earth and Planetary Interiors*, 262:28–40.

[14] Griffith, A. A. (1921). The Phenomena of Rupture and Flow in Solids. *Philosophical Transactions of the Royal Society A: Mathematical, Physical and Engineering Sciences*, 221(582-593):163–198.

[15] Grosfils, E. B., McGovern, P. J., Gregg, P. M., Galgana, G. A., Hurwitz, D. M., Long, S. M., and Chestler, S. R. (2015). Elastic models of magma reservoir mechanics: a key tool for investigating planetary volcanism. *Geological Society, London, Special Publications*, 401(1):239–267.

[16] Head, J. W. (1976). Lunar volcanism in space and time. *Reviews of Geophysics*, 14(2):265–300.

[17] Head, J. W. and Wilson, L. (1992). Lunar mare volcanism: Stratigraphy, eruption conditions, and the evolution of secondary crusts. *Geochimica et Cosmochimica Acta*, 56(6):2155–2175.

[18] Head, J. W. and Wilson, L. (1993). Lunar graben formation due to near-surface deformation accompanying dike emplacement. *Planetary and Space Science*, 41(10):719–727.

[19] Head, J. W. and Wilson, L. (2017). Generation, ascent and eruption of magma on the moon: New insights into source depths, magma supply, intrusions and effusive/explosive eruptions (part 2: Predicted emplacement processes and observations). *Icarus*, 283:176–223.

[20] Hoagland, R. G., Hahn, G. T., and Rosenfield, A. R. (1973). Influence of microstructure on fracture propagation in rock. page 30.

[21] Jozwiak, L. M., Head, J. W., and Wilson, L. (2015). Lunar floor-fractured craters as magmatic intrusions: Geometry, modes of emplacement, associated tectonic and volcanic features, and implications for gravity anomalies. *Icarus*, 248:424–447.

[22] Jozwiak, L. M., Head, J. W., Zuber, M. T., Smith, D. E., and Neumann, G. A. (2012). Lunar floor-fractured craters: Classification, distribution, origin and implications for magmatism and shallow crustal structure: FLOOR-FRACTURED CRATER DISTRIBUTION AND ORIGIN. *Journal of Geophysical Research: Planets*, 117(E11):n/a–n/a.

[23] Lister, J. R. (1990). Buoyancy-driven fluid fracture: similarity solutions for the horizontal and vertical propagation of fluid-filled cracks. *Journal of Fluid Mechanics*, 217:213–239.

[24] Lister, J. R. and Kerr, R. C. (1991). Fluid-mechanical models of crack propagation and their application to magma transport in dykes. *Journal of Geophysical Research*, 96(B6):10049.

[25] Lockner, D. A., Byerlee, J. D., Kuksenko, V., Ponomarev, A., and Sidorin, A. (1991). Quasi-static fault growth and shear fracture energy in granite. *Nature*, 350(6313):39–42.

[26] Maccaferri, F., Richter, N., and Walter, T. R. (2017). The effect of giant lateral collapses on magma pathways and the location of volcanism. *Nature Communications*, 8(1).

[27] Maccaferri, F., Rivalta, E., Keir, D., and Acocella, V. (2014). Off-rift volcanism in rift zones determined by crustal unloading. *Nature Geoscience*, 7(4):297–300.

[28] Maccaferri, F., Smittarello, D., Pinel, V., and Cayol, V. (2019). On the Propagation Path of Magma-Filled Dikes and Hydrofractures: The Competition Between External Stress, Internal Pressure, and Crack Length. *Geochemistry, Geophysics, Geosystems*, 20(4):2064–2081.

[29] Melosh, H. and Ivanov, B. (1999). Impact crater collapse. *Annual Review of Earth and Planetary Sciences*, 27(1):385–415.

[30] Menand, T., Daniels, K. A., and Benghiat, P. (2010). Dyke propagation and sill formation in a compressive tectonic environment. *Journal of Geophysical Research*, 115(B8).

[31] Michaut, C. (2011). Dynamics of magmatic intrusions in the upper crust: Theory and applications to laccoliths on Earth and the Moon. *Journal of Geophysical Research*, 116(B5).

[32] Michaut, C. and Pinel, V. (2018). Magma ascent and eruption triggered by cratering on the moon. *Geophysical Research Letters*, 45(13):6408–6416.

[33] Michaut, C., Pinel, V., and Maccaferri, F. (2020). Magma ascent at floor-fractured craters diagnoses the lithospheric stress state on the moon. *Earth and Planetary Science Letters*, 530:115889.

[34] Muirhead, J. D., Airoldi, G., Rowland, J. V., and White, J. D. L. (2012). Interconnected sills and inclined sheet intrusions control shallow magma transport in the Ferrar large igneous province, Antarctica. *Geological Society of America Bulletin*, 124(1-2):162–180.

[35] Olesiak, Z. and Wnuk, M. (1968). Plastic energy dissipation due to a penny-shaped crack. *International Journal of Fracture Mechanics*, 4(4):383–396.

[36] Orowan, E. (1954). Energy criteria of fracture. Technical report, Massachusetts Inst of Tech Cambridge Dept of Mechanical Engineering.

[37] Pike, R. J. (1977). Size-dependence in the shape of fresh impact craters on the moon. In *Impact and explosion cratering: Planetary and terrestrial implications*, pages 489–509.

[38] Pinel, V. and Jaupart, C. (2000). The effect of edifice load on magma ascent beneath a volcano. *Philosophical Transactions of the Royal Society of London. Series A: Mathematical, Physical and Engineering Sciences*, 358(1770):1515–1532.

[39] Pinel, V. and Jaupart, C. (2005). Some consequences of volcanic edifice destruction for eruption conditions. *Journal of Volcanology and Geothermal Research*, 145(1-2):68–80.

[40] Pollard, D. D. and Johnson, A. M. (1973). Mechanics of growth of some laccolithic intrusions in the henry mountains, utah, ii: bending and failure of overburden layers and sill formation. *Tectonophysics*, 18(3-4):311–354.

[41] Poppe, S., Galland, O., de Winter, N., Goderis, S., Claeys, P., Debaille, V., Boulvais, P., and Kervyn, M. (2020). Structural and geochemical interactions between magma and sedimentary host rock: the hovedøya case, oslo rift, norway. *Geochemistry, Geophysics, Geosystems*, page e2019GC008685.

[42] Poppe, S., Holohan, E. P., Galland, O., Buls, N., Van Gompel, G., Keelson, B., Tournigand, P.-Y., Brancart, J., Hollis, D., Nila, A., and Kervyn, M. (2019). An Inside Perspective on Magma Intrusion: Quantifying 3d Displacement and Strain in Laboratory Experiments by Dynamic X-Ray Computed Tomography. *Frontiers in Earth Science*, 7.

[43] Rice, J. R., Sammis, C. G., and Parsons, R. (2005). Off-Fault Secondary Failure Induced by a Dynamic Slip Pulse. *Bulletin of the Seismological Society of America*, 95(1):109–134.

[44] Richardson, J., Connor, C., Wetmore, P., Connor, L., and Gallant, E. (2015). Role of sills in the development of volcanic fields: Insights from lidar mapping surveys of the San Rafael Swell, Utah. *Geology*, 43(11):1023–1026.

[45] Rivalta, E., Taisne, B., Bunger, A., and Katz, R. (2015). A review of mechanical models of dike propagation: Schools of thought, results and future directions. *Tectonophysics*, 638:1–42.

[46] Roman, A. and Jaupart, C. (2014). The impact of a volcanic edifice on intrusive and eruptive activity. *Earth and Planetary Science Letters*, 408:1–8.

[47] Rubin, A. M. (1995). Propagation of magma-filled cracks. *Annual Review of Earth and Planetary Sciences*, 23(1):287–336.

[48] Sato, H., Kurita, K., and Baratoux, D. (2010). The formation of floor-fractured craters in Xanthe Terra. *Icarus*, 207(1):248–264.

[49] Schultz, P. H. (1976). Floor-fractured lunar craters. *The Moon*, 15(3-4):241–273.

[50] Schultz, P. H. (1978). Martian intrusions: Possible sites and implications. *Geophysical Research Letters*, 5(6):457–460.

[51] Segall, P. (2010). *Earthquake and volcano deformation*. Princeton University Press.

[52] Smith, E. I. (1973). Identification, distribution and significance of lunar volcanic domes. *The moon*, 6(1-2):3–31.

[53] Sneddon, I. N. (1946). The distribution of stress in the neighbourhood of a crack in an elastic solid. *Proceedings of the Royal Society of London. Series A. Mathematical and Physical Sciences*, 187(1009):229–260.

[54] Sneddon, I. N. (1995). *Fourier transforms*. Courier Corporation.

[55] Spacapan, J. B., Galland, O., Leanza, H. A., and Planke, S. (2017). Igneous sill and finger emplacement mechanism in shale-dominated formations: a field study at Cuesta del Chihuido, Neuquén Basin, Argentina. *Journal of the Geological Society*, 174(3):422–433.

[56] Taisne, B. and Jaupart, C. (2009). Dike propagation through layered rocks. *Journal of Geophysical Research*, 114(B9).

[57] Thorey, C. and Michaut, C. (2014). A model for the dynamics of crater-centered intrusion: Application to lunar floor-fractured craters. *Journal of Geophysical Research: Planets*, 119(1):286–312.

[58] Thorey, C., Michaut, C., and Wieczorek, M. (2015). Gravitational signatures of lunar floor-fractured craters. *Earth and Planetary Science Letters*, 424:269–279.

[59] Timošenko, S. P. and Goodier, J. N. (1951). *Theory of elasticity*. McGraw-Hill.

[60] Timoshenko, S. P. and Woinowsky-Krieger, S. (1959). *Theory of plates and shells*. McGraw-hill.

[61] Tinti, E., Spudich, P., and Cocco, M. (2005). Earthquake fracture energy inferred from kinematic rupture models on extended faults. *Journal of Geophysical Research*, 110(B12).

[62] Vandenberghe, N., Vermorel, R., and Villermaux, E. (2013). Star-shaped crack pattern of broken windows. *Physical review letters*, 110(17):174302.

[63] Walker, G. P. L. (1989). Gravitational (density) controls on volcanism, magma chambers and intrusions. *Australian Journal of Earth Sciences*, 36(2):149–165.

[64] Watanabe, T., Masuyama, T., Nagaoka, K., and Tahara, T. (2002). Analog experiments on magma-filled cracks: Competition between external stresses and internal pressure. *Earth, Planets and Space*, 54(12):e1247–e1261.

[65] Weertman, J. (1971). Theory of water-filled crevasses in glaciers applied to vertical magma transport beneath oceanic ridges. *Journal of Geophysical Research*, 76(5):1171–1183.

[66] Wichman, R. and Schultz, P. (1996). Crater-Centered Laccoliths on the Moon: Modeling Intrusion Depth and Magmatic Pressure at the Crater Taruntius. *Icarus*, 122(1):193–199.

[67] Wichman, R. W. and Schultz, P. H. (1995). Floor-fractured impact craters on Venus: Implications for igneous crater modification and local magmatism. *Journal of Geophysical Research*, 100(E2):3233.

[68] Wieczorek, M. A., Neumann, G. A., Nimmo, F., Kiefer, W. S., Taylor, G. J., Melosh, H. J., Phillips, R. J., Solomon, S. C., Andrews-Hanna, J. C., Asmar, S. W., Konopliv, A. S., Lemoine, F. G., Smith, D. E., Watkins, M. M., Williams, J. G., and Zuber, M. T. (2013). The Crust of the Moon as Seen by GRAIL. *Science*, 339(6120):671–675.

[69] Wieczorek, M. A., Zuber, M. T., and Phillips, R. J. (2001). The role of magma buoyancy on the eruption of lunar basalts. *Earth and Planetary Science Letters*, 185(1-2):71–83.

[70] Wöhler, C., Lena, R., and Group, G. L. R. G. (2009). Lunar intrusive domes: Morphometric analysis and laccolith modelling. *Icarus*, 204(2):381–398.

[71] Wong, T.-f. (1982). Shear fracture energy of Westerly granite from post-failure behavior. *Journal of Geophysical Research: Solid Earth*, 87(B2):990–1000.